

考虑晶粒不均匀性的不锈钢激光淬火数值模拟

陈正威, 李昌*, 高兴, 高鹤芯, 韩兴

辽宁科技大学机械工程与自动化学院, 辽宁 鞍山 114051

摘要 淬火基体中的微观晶粒不均匀性对于揭示激光淬火机理、提高淬火质量具有重要意义。基于 Voronoi 法建立了淬火基体的随机微晶组织模型,通过对纳米压痕实验的统计分析引入了淬火基体晶粒的不均匀性,确定了晶粒不均匀分布特性并划分了晶粒类型。由晶粒不均匀系数确定各类晶粒的材料属性。利用 Python 脚本程序将不同的材料属性按照概率随机赋予 Voronoi 元胞。建立了考虑晶粒不均匀性的 SUS301L-HT 不锈钢激光淬火过程热力耦合模型。计算了激光淬火温度场和热应力场,计算结果表明:晶粒不均匀性导致淬火基体应力呈现明显的不均匀性分布,基体内部相邻晶粒边界处的应力发生突变,且晶粒间的力学性能差异越大,突变现象越显著。考虑晶粒不均匀性建立的激光淬火模型为揭示激光淬火过程微观演变机理提供了一种有效方法。

关键词 激光技术; 激光淬火; 晶粒不均匀性; 不锈钢; Voronoi 模型

中图分类号 TG156.3

文献标志码 A

doi: 10.3788/CJL202148.1002109

1 引言

激光淬火又称激光表面硬化,它利用高密度能量的激光束照射钢材表面,钢材迅速被加热到相变点以上的温度,然后迅速冷却,从而在基体表面获得淬硬层但不改变基体内部力学性能^[1],激光淬火原理图如图 1 所示。该工艺具有热变形及应力小、工艺周期短、质量稳定可控和处理效率高等优点^[2-3]。激光淬火处理可有效提高零件表面耐磨性、耐腐蚀性、耐疲劳性^[4-6]。激光淬火因其独有的优势,得到了广泛的关注。

随着激光加工技术的发展,大功率激光器的需求不断增加。在激光器功率提高的同时激光器产热也随着增加,从而影响激光器的性能。为了促进激光器的工业化发展,许多学者致力于提高激光器工作稳定性的研究。赵碧瑶等^[7]对激光器工作时的温度场进行了数值分析,为激光器引入了边缘绝热封装方式,削弱了激光器芯片工作时的温度不均匀性,进而提高了激光光束的质量。吕坤鹏等^[8]基于流-

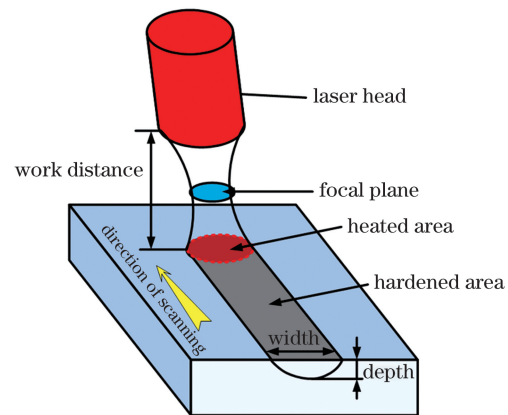


图 1 激光淬火原理图

Fig. 1 Schematic of laser quenching

固-热耦合的数值模拟方法分析了不同冷却条件下激光器的温度场分布,为激光器冷却结构的改进提供了理论依据。余霞等^[9]调研发现光纤激光具有操作方便、散热要求低、光束质量好、功率高等优势,具有很好的应用前景。王世杰等^[10]利用国产光纤实现了光纤激光器的搭建。学者们的共同努力为激光加工

收稿日期: 2020-08-21; **修回日期:** 2020-09-25; **录用日期:** 2020-11-05

基金项目: 国家自然科学基金(51105187)、辽宁省自然科学基金指导计划项目(2019ZD0277)、天津市重点研发计划科技支撑重点项目(S20ZC771198)、公安部武警消防重点实验室开放课题(KF201704)、辽宁科技大学创新团队建设基金项目(601009830-2)

*E-mail: lichang2323-23@163.com

技术的发展提供了保障,促使激光淬火及其他激光加工技术被广泛应用于汽车、航空航天、模具等领域。

2014 年, Li 等^[11]通过实验与数值分析研究了激光功率、扫描速度等工艺参数对淬火层组织、深度及硬度的影响,并比较了高功率二极管激光器和二氧化碳激光器两种工业激光器对 AISI1045 钢激光淬火的影响。2018 年, Hung 等^[12]通过建立 AISI 1045 和 AISI 4140 钢表面硬化过程热力耦合有限元模型,研究了激光功率、扫描速度和激光光斑尺寸等参数对单轨激光表面处理过程中表面温度分布、硬化宽度和深度的影响。2019 年, Khorram 等^[13]利用 Nd:YAG 激光对 Ti-5Al-2.5Sn 合金进行了表面硬化,研究了激光频率、激光脉冲宽度、激光扫描速度和焦点位置等激光参数对硬化区微观结构、几何尺寸的影响。张群莉等^[14]利用 COMSOL Multiphysics 软件对 42CrMo 钢激光淬火过程中的温度场进行了分析,研究了相同功率下光斑的几何尺寸对硬化层的影响。郭卫等^[15]通过 ANSYS 软件模拟并结合实验,研究了激光功率对 27SiMn 钢激光淬火处理的影响。2020 年, 陈凯焯等^[16]通过实验与数值模拟,研究了传统激光淬火与振镜扫描式激光淬火两种方式的温度变化特性和规律。Alikhani 等^[17]通过数值分析的方法,分析了 AISI4130 钢的大功率二极管激光表面硬化的热过程。

虽然许多学者已经对激光淬火及相关领域进行

了很多研究,但是目前该领域的研究主要集中于激光淬火温度场、应力场分布特点的分析,激光淬火工艺参数对淬火质量影响的分析,淬硬层厚度预测等方面。激光淬火过程中基体内的微观组织瞬时变化,晶粒的最终状态决定了淬火基体的力学性能,微观组织结构特征的优化是实现力学性能精确调控的关键^[18-20]。然而现有的实验测量手段和数值模拟方法都难以获得淬火过程中基体内晶粒的应力变化状态。为了能有效捕捉激光淬火过程中微观晶粒的演变规律,本文提出了一种以 Voronoi 模型表征晶粒随机结构,以纳米压痕实验结果划分晶粒类别的激光淬火热力耦合数值分析模型,用于捕捉淬火过程中基体内部的晶粒温度、应力变化信息。

2 不锈钢激光淬火数值模拟

2.1 材料属性

以 SUS301L-HT 不锈钢作为基体,模型尺寸为 40 mm×35 mm×3 mm,其密度为 7800 kg·m⁻³,潜热为 2.6×10⁵ J·kg⁻¹,固相线温度为 1350 K,液相线温度为 1723 K,波尔兹曼常数为 5.67×10⁻⁸ W·(m²·K⁴)⁻¹,基体发射率为 0.8,对流换热系数为 20 W·(m²·K),基体其他温变物性参数选取如表 1^[21]所示,其中 T₁ 为温度, k 为热导率, c 为比热容, E 为弹性模量, σ_s 为屈服极限, β 为热膨胀系数。

表 1 SUS301L-HT 不锈钢的物性参数

Table 1 Physical parameters of SUS301L-HT stainless steel

Thermophysical performance parameter			Mechanical performance parameter			
T ₁ /K	k/[W·(m·K) ⁻¹]	c/[10 ² J·(kg·K) ⁻¹]	T ₁ /K	E/MPa	σ _s /MPa	β/(10 ⁻⁵ K ⁻¹)
293	12.943	4.13	293	60527	821	1.7
473	15.029	4.54	473	66290	771.7	1.73
577	18.334	5.05	673	59093	529.3	1.77
872	20.944	5.5	873	55873	529	1.82
1065	23.318	5.52	1073	37473	296	1.9
1280	26.591	6.0	1273	20103	60	2.0
1380	27.324	5.79				

2.2 热源模型及基本方程

采用高斯面热源模型表征激光热源,热源模型^[11]为

$$q = \eta \frac{2Q}{\pi r_0^2} \exp\left[-\frac{2(x^2 + y^2)}{r_0^2}\right], \quad (1)$$

式中: Q 为激光功率; r₀ 为热源半径; η 为热效率, η=0.85; (x, y) 为点坐标。

激光淬火过程的能量传递遵循热力学第一定

律,热量传递包括热传导、热对流和热辐射三种形式^[22-23]。热传导用傅里叶定律描述:

$$q = -k \nabla \cdot T, \quad (2)$$

热对流由牛顿定律描述:

$$q_c^* = -a_c(T - T_0), \quad (3)$$

热辐射由 Stefan-Boltzmann 定律描述:

$$q_r^* = -\epsilon C_0(T^4 - T_0^4), \quad (4)$$

式中: ε 为基体表面反射率; C₀ 为波尔兹曼(Stefan-

Boltzmann) 常量; a_c 为热对流系数; T_0 为室温, 本文取 $T_0 = 293 \text{ K}$; T 为基体表面温度。

在激光淬火过程中, 基体的总应变包含弹性应变 $d\epsilon^E$ 、塑性应变 $d\epsilon^P$ 和热应变 $d\epsilon^T$:

$$d\epsilon = d\epsilon^E + d\epsilon^P + d\epsilon^T. \quad (5)$$

其中弹性应变根据胡克定律计算, 塑性应服从 Mises 屈服准则, 热应变根据热膨胀系数计算。

采用牛顿法求解非线性热力直接耦合, 耦合方程的矩阵表示为

$$\begin{bmatrix} \mathbf{K}_{uu} & \mathbf{K}_{u\theta} \\ \mathbf{K}_{\theta u} & \mathbf{K}_{\theta\theta} \end{bmatrix} \begin{bmatrix} \Delta u \\ \Delta \theta \end{bmatrix} = \begin{bmatrix} \mathbf{R}_u \\ \mathbf{R}_\theta \end{bmatrix}, \quad (6)$$

式中: Δu 和 $\Delta \theta$ 分别为位移和温度增量; \mathbf{K}_{uu} 、 $\mathbf{K}_{u\theta}$ 、 $\mathbf{K}_{\theta u}$ 、 $\mathbf{K}_{\theta\theta}$ 是全耦合雅可比矩阵的子矩阵; \mathbf{R}_u 和 \mathbf{R}_θ 分别为力和热的残差向量。

2.3 晶粒不均匀性模型的建立

Voronoi 模型是用于表征微观组织随机结构的常用模型, 其二维定义为: 平面 S 上有 n 个不相同的点集合, 满足

$$V(P_h) = \{P \mid d(P, P_h) < d(P, P_l)\}, \quad (7)$$

$$h, l = 1, 2, \dots, n \text{ and } h \neq l,$$

式中: $d(P, P_h)$ 表示点 P 与点 P_h 之间的欧氏距离; 集合 $V(P_h)$ 为点 P_h 所对应的 Voronoi 多边形^[24]。集合 S 中的每一个点生成一个 Voronoi 多边形以组合成 Voronoi 模型。

本文通过开源软件 Neper 生成三维 Voronoi 多晶体模型并将其作为基体几何模型, 模型中的 Voronoi 元胞的数量在保证计算机计算效率的前提下应尽量多, 本文模型包含 3000 个 Voronoi 元胞, 如图 2 所示。

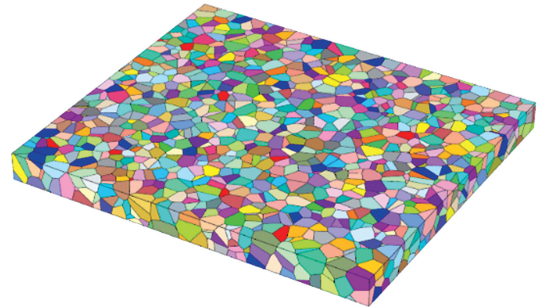


图 2 基于 Voronoi 法建立的激光淬火基体三维模型
Fig. 2 3D model of laser quenching substrate based on Voronoi method

硬度是材料抵抗压痕所产生的塑性变形能力^[20,25]。对未进行激光淬火的 SUS301L-HT 不锈钢试件表面进行砂纸打磨、抛光, 以满足纳米压痕测试要求。采用盐酸+硝酸混合溶液对试件表面进行腐蚀处理, 按图 3(a)所示压痕位置在未淬火基体内选取 12 个晶粒, 利用 Keysight Nano Indenter G200 纳米压痕仪进行纳米压痕测试, 共测试 48 个点。压痕实际测量点如图 3(b)~(d)所示, 各点测量结果如表 2 所示。

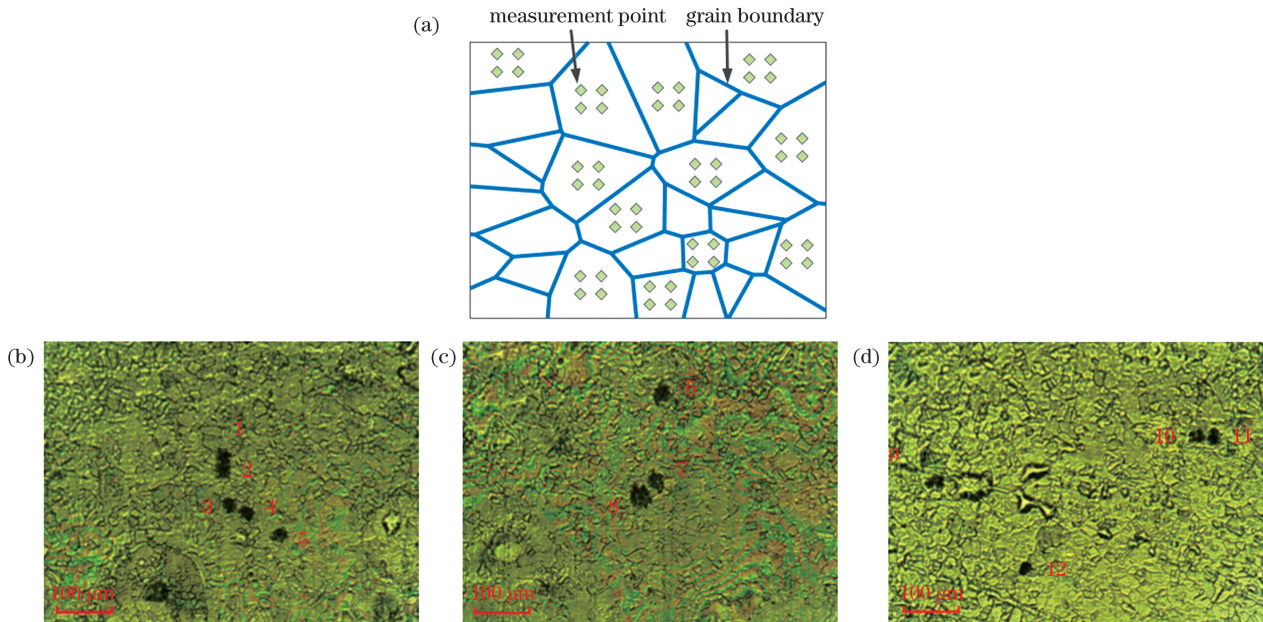


图 3 纳米压痕测量位置。(a)示意图;(b)~(d)实际测量位置
Fig. 3 Locations of nano-indentation measurement. (a) Schematic; (b)~(d)real measurement locations

表 2 纳米压痕实验结果

Table 2 Test results of nano-indentation

Grain	Stress at point 1 /GPa	Stress at point 2 /GPa	Stress at point 3 /GPa	Stress at point 4 /GPa
No. 1	2.89	3.48	4.79	2.09
No. 2	3.93	3.26	3.96	3.83
No. 3	3.52	5.08	2.45	4.81
No. 4	1.90	4.19	3.87	5.78
No. 5	6.22	3.32	4.49	3.41
No. 6	3.85	4.95	0.98	5.15
No. 7	3.48	3.58	5.01	3.53
No. 8	2.12	4.94	5.74	4.97
No. 9	5.89	2.81	1.91	4.29
No. 10	3.54	5.35	3.51	4.44
No. 11	5.06	2.39	5.91	3.27
No. 12	3.34	3.91	3.80	3.23

根据纳米压痕结果发现不同晶粒具有不同的力学性能,计算出表征晶粒力学性能不均匀性的系数 ξ :

$$\xi = \frac{H_{i'}}{H_m}, \quad (8)$$

式中: ξ 为晶粒不均匀性系数; $H_{i'}$ 为第*i'*个晶粒硬度值; H_m 为晶粒硬度均值。

对晶粒不均匀系数进行统计分析,晶粒不均匀系数呈正态分布(均值 $\mu_1 = 1$, 标准差 $\sigma_1 = 0.318724$),统计结果如图 4(a)所示。根据晶粒不均匀性系数 ξ ,可将晶粒划分为 7 类,各类晶粒的力学性能为

$$\sigma_i = \xi\sigma, \quad (9)$$

式中: σ_i 为第*i*类晶粒流动应力; σ 为基体流动应力。

考虑到纳米压痕实验选取样本空间和实验测试时会引入误差,所以必须对 ξ 的分布进行标准化处理,结果如图 4(b)所示,然后利用 Python 脚本程序

将每类晶粒的流动应力 σ_i 按图 5(a)所示流程随机赋给各 Voronoi 元胞^[26-27],其中 N 为模型中 Voronoi 元胞总数, N_i 为第*i*类晶粒所对应的 Voronoi 元胞数量, P_i 为第*i*类晶粒出现的概率, j 为循环变量,表示已获得第*i*类材料属性的 Voronoi 元胞数。结果如图 5(b)所示,从而建立了考虑晶粒不均匀性的激光淬火基体模型。

2.4 有限元模型的建立及求解

基于上述方法建立考虑晶粒不均匀性的基体模型。对基体平行于扫描轨迹的两侧施加位移约束,利用 Fortran 子程序施加移动的激光热源,对单道激光淬火过程进行分析。本文中激光功率为 1000 W,激光光斑半径为 3 mm,激光扫描速度 $v = 50$ mm/s。建立考虑晶粒不均匀性的激光淬火模型,如图 6(a)所示,模型选用八节点实体单元 C3D8T,模型包含 316966 个节点,288840 个单元。模型的建立及求解流程如图 6(b)所示。

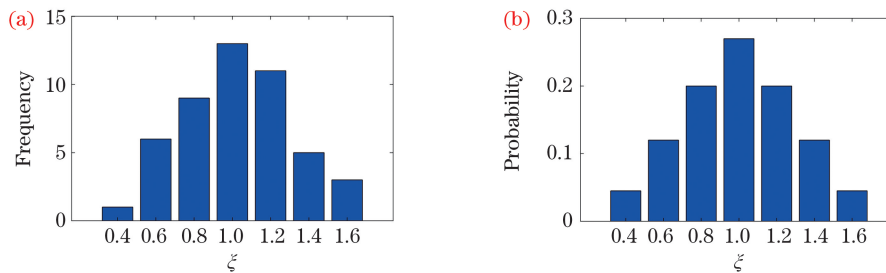


图 4 晶粒不均匀系数分布图。(a)统计结果;(b)标准化结果

Fig. 4 Distribution of grain non-uniformity coefficient. (a) Statistical result; (b) standardization result

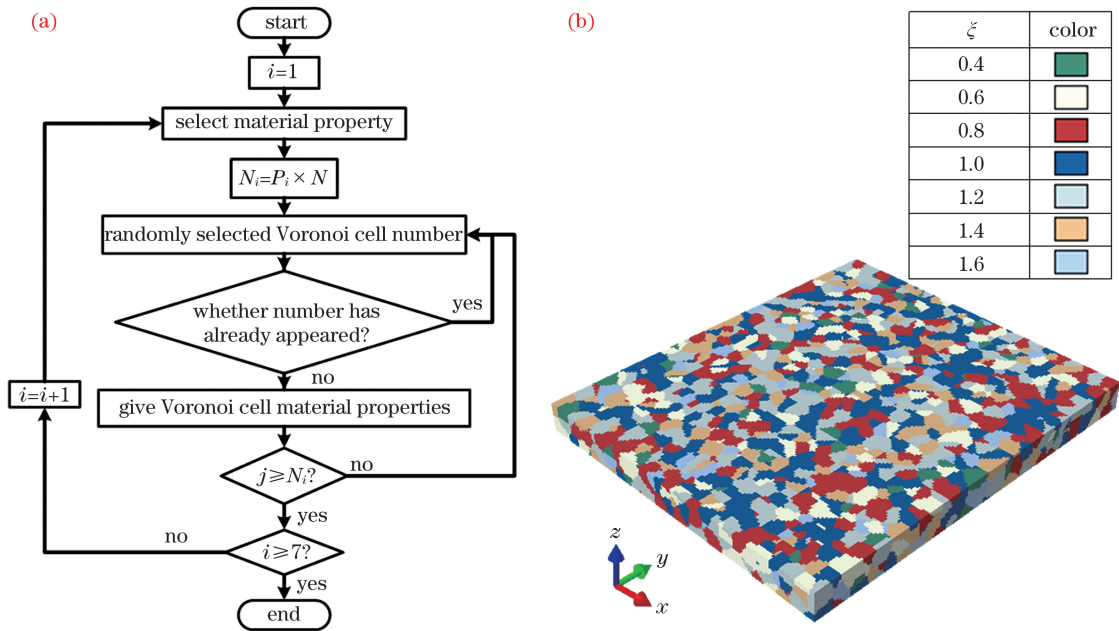


图 5 晶粒异质性的引入方法及结果。(a)程序流程图;(b)考虑晶粒非均匀性的三维激光淬火基体模型
Fig. 5 Introduction method of grain heterogeneity and result. (a) Flow chart of program; (b) 3D model of laser quenching substrate with grain heterogeneity

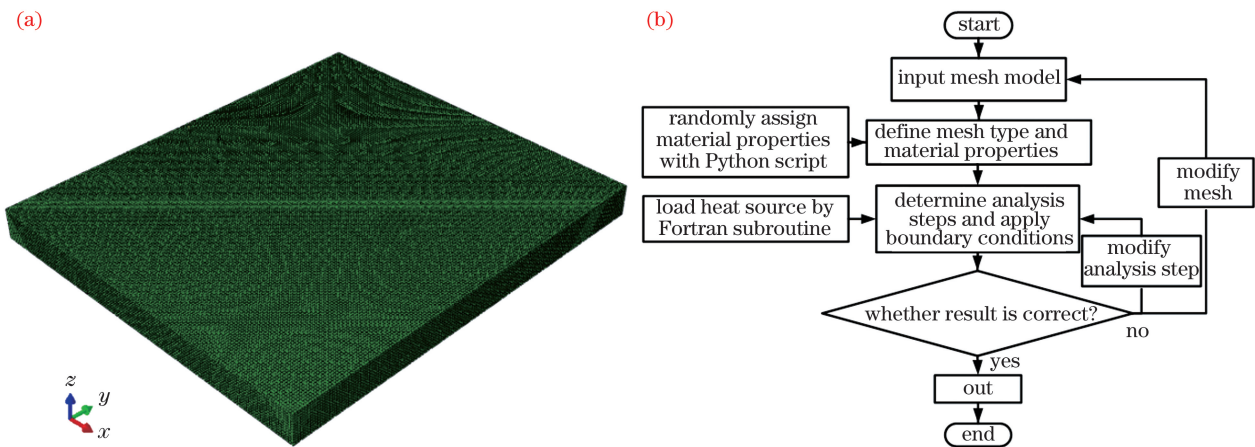


图 6 考虑晶粒不均匀性的激光淬火有限元模型及其计算流程图。(a)有限元模型;(b)计算流程图
Fig. 6 Finite element model of laser quenching with grain heterogeneity and its calculation process. (a) Finite element model; (b) calculation process

3 结果与分析

激光淬火过程中不同时刻的温度场分布如图 7 所示,图 8 为有限元计算结果与实验结果的对比。计算结果表明:基体在热源的作用下迅速升温并达到高温,淬火最高温度接近 1669.3 K。基体内温度场以热传导方式由光斑向四周扩散,该过程同时受热辐射、热对流和热传导的综合作用,故基体温度由热源中心向外呈梯度递减,基体温度场沿扫描方向呈对称分布。热源后方在热传导作用下持续输入热

量,导致该区域温度降低的速度较慢,因此呈现热源前端温度变化梯度大于后端温度变化梯度。淬火完成区的温度在热传导、热对流及热辐射的综合作用下呈“彗星状”,导致热源前端的温度变化梯度明显大于热源后方的温度变化梯度。完成淬火的基体温度迅速降低,自然冷却 300 s 后,基体各处的温度趋于一致,接近室温,此时可认为淬火基体已完成冷却过程。实验结果与模型计算结果吻合良好,证明了模型的有效性。激光淬火的温度场变化表明激光淬火冷却迅速。

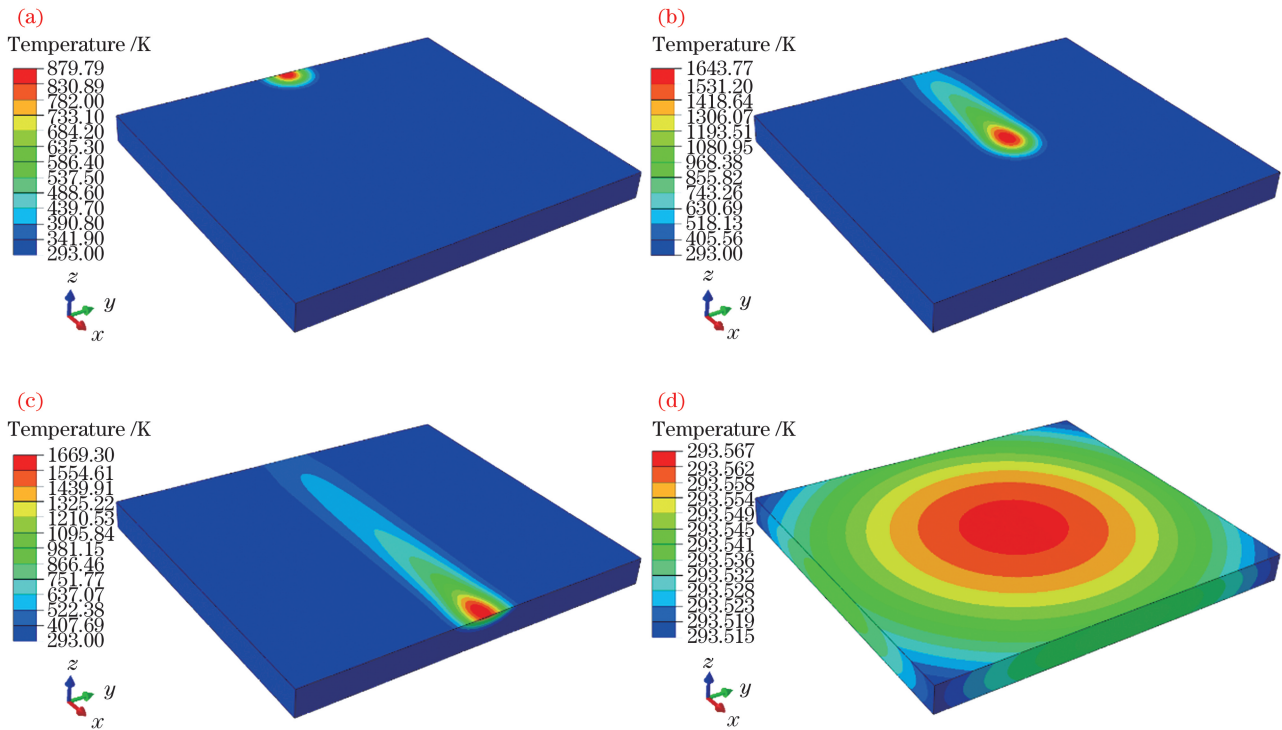


图 7 淬火基体在不同时刻的温度场分布。(a) 0.01 s; (b) 0.35 s; (c) 0.7 s; (d) 自然冷却 300 s 后

Fig. 7 Temperature distributions in quenching substrate at different quenching moments. (a) 0.01 s; (b) 0.35 s; (c) 0.7 s; (d) after natural cooling for 300 s

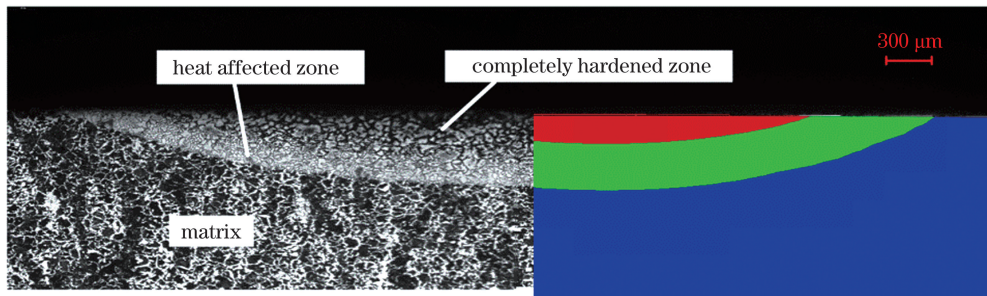


图 8 截面内温度分布与实验结果的比较

Fig. 8 Comparison of temperature distribution in cross section with experimental result

激光淬火过程中不同时刻的热应力分布如图 9 所示。基体在热源作用下产生热应力,热应力从热源处向外扩散,热应力场与温度场呈现类似分布,但由于热源中心处的温度最高,该区域内金属的力学性能受高温影响而减弱,因此热源中心处的热应力较小。由于模型考虑了晶粒不均匀性,基体的热应力分布出现了与晶粒随机几何分布相似的不均匀分布,即热应力的等值线会因晶粒的随机几何结构而呈现不规则分布。这是因为在相同热输入下,基体内的晶粒具有不同的力学性能,所以晶粒产生了不同的热应力,当相邻晶粒具有不同的力学性能时,晶界处出现应力突变。由于基体中有少部分晶粒具有较强的力学性能,在激光照射下,该部分晶粒出现了

高于平均水平的热应力,达 1429 MPa;而基体大部分晶粒的应力水平在 600 MPa 左右。因此,这部分具有较高热应力的晶粒仅表征了晶粒自身的热应力状态,而对基体整体的热应力状态的贡献较小。

在基体内选取 A、B、C、D 四个晶粒,晶粒位置如图 10(a)所示。晶粒 A、B、C、D 的温度变化曲线如图 10(b)所示。晶粒 A、B、C、D 的热应力变化曲线如图 10(c)所示。晶粒 A 和 B 位于扫描轨迹内,晶粒 A 在激光扫描侧,晶粒 B 在激光扫描背侧,晶粒 C、D 逐渐远离激光扫描轨迹。受热传递的影响,当热源接近时,位于基体内的晶粒迅速产生峰值温度,同时产生热应力,峰值温度的大小与到热源的距离呈负相关,热应力与热影响效果呈正相关。晶粒

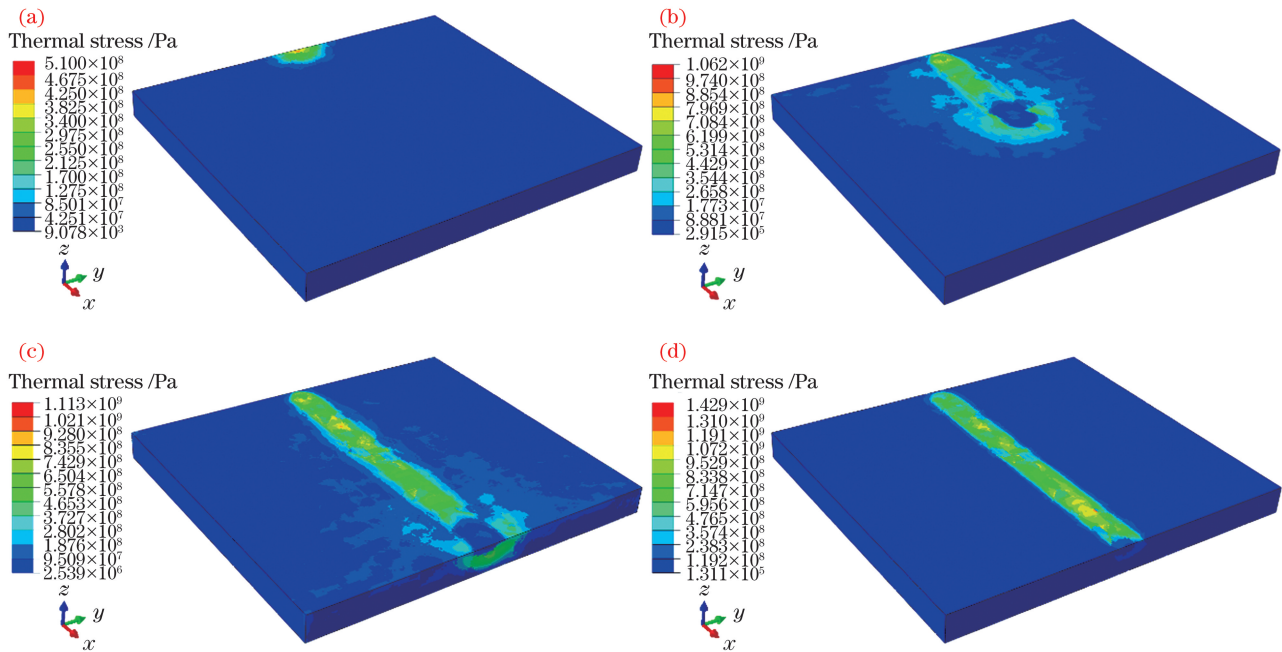


图 9 考虑晶粒不均匀性的激光淬火模型在不同时刻的热应力分布。(a) 0.01 s; (b) 0.35 s; (c) 0.7 s; (d) 自然冷却 300 s 后
 Fig. 9 Thermal stress distributions of laser quenching model with grain heterogeneity at different moments. (a) 0.01 s; (b) 0.35 s; (c) 0.7 s; (d) after natural cooling for 300 s

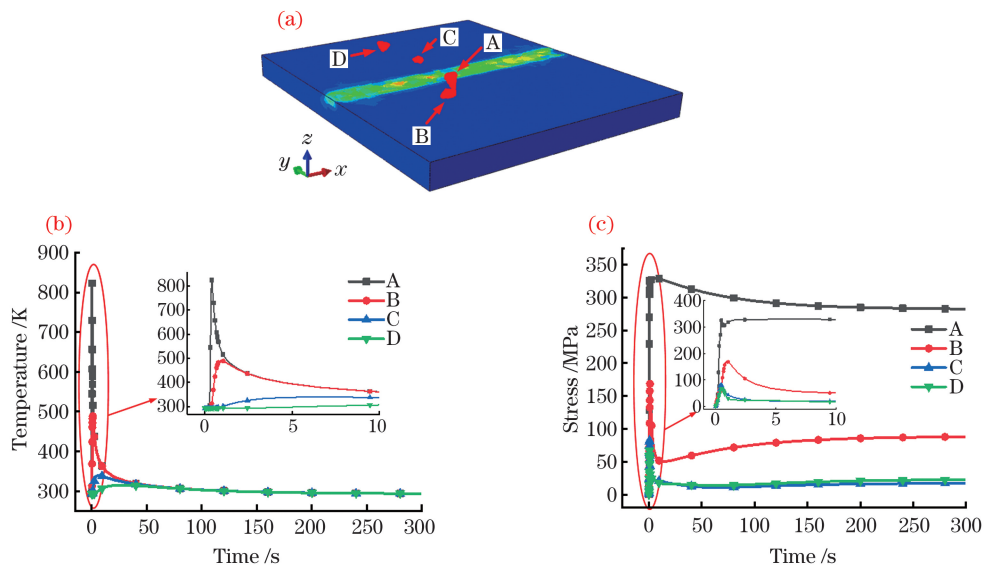


图 10 激光淬火过程中晶粒的温度和热应力变化曲线。(a) 晶粒位置示意图; (b) 晶粒温度的变化曲线; (c) 晶粒热应力的变化曲线

Fig. 10 Temperature and thermal stress curves of grains during laser quenching. (a) Schematic of grain locations; (b) grain temperature versus time; (c) thermal stress versus time

A、B 与激光热源的距离相对较小,即受激光热源的作用效果较大,所以当热源接近晶粒所处位置时,晶粒 A、B 的温升梯度、峰值温度及热应力均高于晶粒 C、D。因为晶粒 B 处于激光扫描背侧,所受影响低于晶粒 A,所以晶粒 A 的温升梯度、峰值温度及热应力均大于晶粒 B、C、D。当热源离开后,各晶粒的温度迅速降低,晶粒的热应力也出现减小趋势。但

位于激光扫描轨迹正面的晶粒 A 在热源离开后,在热传递的作用下仍会出现一定的增长,热源距离其位置较远时热应力才会呈现减小趋势。晶粒的温度变化曲线也进一步验证了热源前端的温度变化梯度大于热源后端的温度变化梯度。由于此处所选取的四个晶粒均不具有较强的力学性能,因此这四个晶粒的应力峰值远低于淬火过程中出现的应力峰值。

图 11(a) 为所选取晶粒在基体中的位置及各晶粒的力学性能分类。图 11(b) 为激光淬火基体自然冷却 300 s 后局部晶粒的热应力云图。考虑晶粒不均匀性模型的计算结果很好地揭示了晶粒在晶界处的热应力变化。由于晶粒的不均匀性, 晶体的热应力会在晶界处发生应力突变, 相邻两个晶粒的力学性能差距越大, 应力突变现象越显

著。如晶粒 7 ($\xi=0.6$) 与晶粒 10 ($\xi=1.6$) 之间的应力突变明显大于晶粒 ($\xi=1.2$) 2 与晶粒 4 ($\xi=1$); 晶粒 8 ($\xi=0.8$) 与晶粒 2 ($\xi=1.2$) 之间的应力突变明显大于晶粒 8 ($\xi=0.8$) 与晶粒 1 ($\xi=1$); 晶粒 3 ($\xi=1$) 与晶粒 4 ($\xi=1$) 具有相同的力学性能, 所以在晶粒 3 与晶粒 4 的晶界处不存在应力突变。

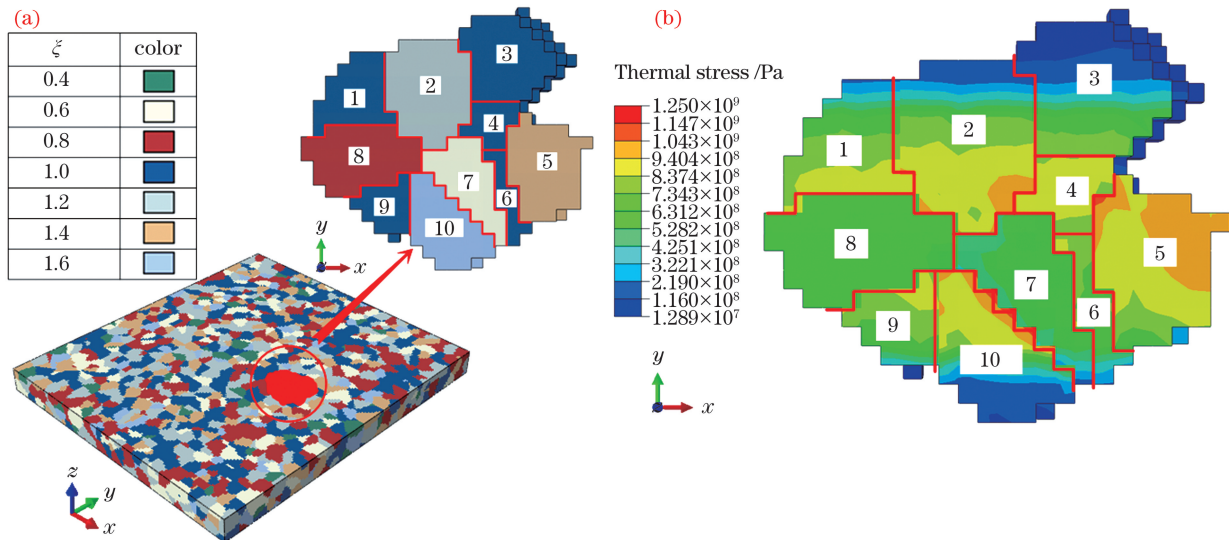


图 11 应力在局部晶粒中的分布。(a) 所选取的晶粒位置及晶粒力学性能; (b) 所选取的晶粒的应力分布

Fig. 11 Stress distributions in local grains. (a) Positions and mechanical properties of selected grains; (b) stress distribution in selected grains

4 结 论

采用 Voronoi 法建立了淬火基体随机多晶组织模型, 根据纳米压痕实验结果引入了晶粒不均匀性, 在 ABAQUS 平台上建立了考虑晶粒不均匀性的激光淬火数值分析模型, 并计算了激光淬火过程中的温度场和热应力场。由于基体内部晶粒的力学性能存在不均匀性, 因此晶粒应力在晶界处出现突变, 相邻晶粒之间的力学性能差距越大, 晶界应力突变越明显。基体热应力分布等值线与晶粒随机结构呈相似的不规则分布。

参 考 文 献

- [1] Liu C G, Qiu X W. Laser hardening surface treatment technology and its present application[J]. Rare Metals and Cemented Carbides, 2012, 40(1): 62-64.
刘春阁, 邱星武. 激光硬化表面处理技术及其应用现状[J]. 稀有金属与硬质合金, 2012, 40(1): 62-64.
- [2] Pan L, Tao X Q, Xia C H, et al. Study on laser surface hardening for sealing face and its application [J]. Heat Treatment of Metals, 2002, 27(1): 18-20.
- [3] Qin Z B, Wu Z, Hu W B, et al. Application and progress of surface engineering technology[J]. The Chinese Journal of Nonferrous Metals, 2019, 29(9): 2192-2216.
秦真波, 吴忠, 胡文彬, 等. 表面工程技术的应用及其研究现状[J]. 中国有色金属学报, 2019, 29(9): 2192-2216.
- [4] Yang Z, Fan X F, Qiu C J, et al. Microstructure and properties of 40CrNiMoA steel surface after laser quenching [J]. Laser & Optoelectronics Progress, 2020, 57(1): 011405.
杨振, 樊湘芳, 邱长军, 等. 40CrNiMoA 钢表面激光淬火后的组织和性能[J]. 激光与光电子学进展, 2020, 57(1): 011405.
- [5] Huang J Y, Shen Z J, Zhang L X, et al. Applications of laser surface treatment technologies in petroleum machinery [J]. Laser & Optoelectronics Progress, 2019, 56(6): 060005.
黄俊媛, 沈泽俊, 张立新, 等. 激光表面处理技术在石油机械中的应用[J]. 激光与光电子学进展, 2019, 56(6): 060005.
- [6] Wang Y S, Zhang X Q, Lei J B, et al. Processing of

- laser quenching crankshaft [J]. Chinese Journal of Lasers, 2007, 34(4): 574-576.
- 王云山, 张兴泉, 雷剑波, 等. 曲轴激光淬火工艺 [J]. 中国激光, 2007, 34(4): 574-576.
- [7] Zhao B Y, Jing H Q, Zhong L, et al. Improving slow-axis laser beam quality of semiconductor laser with edge adiabatic package [J]. Chinese Journal of Lasers, 2020, 47(1): 0105002.
- 赵碧瑶, 井红旗, 仲莉, 等. 半导体激光器边缘绝热封装改善慢轴光束质量 [J]. 中国激光, 2020, 47(1): 0105002.
- [8] Lü K P, Liu Z Y, Yang X, et al. Numerical research on microchannel cooling structure of high power solid-state lasers [J]. Chinese Journal of Lasers, 2020, 47(6): 0601010.
- 吕坤鹏, 刘震宇, 杨雪, 等. 高功率固体激光器微通道冷却结构的数值研究 [J]. 中国激光, 2020, 47(6): 0601010.
- [9] Yu X, Luo J Q, Xiao X S, et al. Research progress of high-power ultrafast fiber lasers [J]. Chinese Journal of Lasers, 2019, 46(5): 0508007.
- 余霞, 罗佳琪, 肖晓晟, 等. 高功率超快光纤激光器研究进展 [J]. 中国激光, 2019, 46(5): 0508007.
- [10] Wang S J, Zhang Z L, Cao C, et al. Nanosecond pulse laser output with average power of 761 W and pulse energy of 17.5 mJ based on domestic fiber [J]. Chinese Journal of Lasers, 2019, 46(12): 1215002.
- 王世杰, 张志伦, 曹驰, 等. 利用国产光纤实现平均功率 761 W、脉冲能量 17.5 mJ 纳秒脉冲激光输出 [J]. 中国激光, 2019, 46(12): 1215002.
- [11] Li R F, Jin Y J, Li Z G, et al. A comparative study of high-power diode laser and CO₂ laser surface hardening of AISI 1045 steel [J]. Journal of Materials Engineering and Performance, 2014, 23(9): 3085-3091.
- [12] Hung T P, Shi H E, Kuang J H, et al. Temperature modeling of AISI 1045 steel during surface hardening processes [J]. Materials, 2018, 11(10): E1815.
- [13] Khorram A, Jamaloei A D, Jafari A, et al. Surface transformation hardening of Ti-5Al-2.5Sn alloy by pulsed Nd:YAG laser: an experimental study [J]. The International Journal of Advanced Manufacturing Technology, 2019, 100(9/10/11/12): 3085-3099.
- [14] Zhang Q L, Tong W H, Chen Z J, et al. Effect of spot size on geometrical characteristics of laser deep quenching hardened layer of 42CrMo steel [J]. Surface Technology, 2020, 49(1): 254-261.
- 张群莉, 童文华, 陈智君, 等. 光斑尺寸对 42CrMo 钢激光深层淬火硬化层几何特征的影响 [J]. 表面技术, 2020, 49(1): 254-261.
- [15] Guo W, Zhang H J, Chai R X, et al. Numerical simulation and experimental verification of laser quenching on 27SiMn steel surface [J]. Applied Laser, 2019, 39(3): 482-489.
- 郭卫, 张汉杰, 柴蓉霞, 等. 27SiMn 钢表面激光淬火数值模拟及实验验证 [J]. 应用激光, 2019, 39(3): 482-489.
- [16] Chen K Y, Wang Y, Wu G L, et al. Simulation and experiment of laser quenching temperature characteristics based on galvanometer scanning [J]. Surface Technology, 2020, 49(5): 251-258.
- 陈凯焯, 王晔, 吴国龙, 等. 基于扫描振镜的激光淬火温度特性模拟与实验研究 [J]. 表面技术, 2020, 49(5): 251-258.
- [17] Alikhani S T, Zahabi M K, Torkamany M J, et al. Time-dependent 3D modeling of the thermal analysis of the high-power diode laser hardening process [J]. Optics & Laser Technology, 2020, 128: 106216.
- [18] Kong D J, Zhang L, Song R G, et al. Effect of laser quenching on fatigue properties and fracture morphologies of 40CrNiMo high strength steel [J]. Chinese Journal of Lasers, 2013, 40(11): 1103005.
- 孔德军, 张垒, 宋仁国, 等. 激光淬火对 40CrNiMo 高强度钢疲劳性能与断口形貌的影响 [J]. 中国激光, 2013, 40(11): 1103005.
- [19] Li S C, Mo B, Xiao G, et al. The microstructure characteristics and their influence factors during laser additive manufacturing of metal materials [J]. Laser & Optoelectronics Progress, 2021, 58(1): 0100007.
- 李时春, 莫彬, 肖罡, 等. 金属材料的激光增材制造微观组织结构特征及其影响因素 [J]. 激光与光电子学进展, 2021, 58(1): 0100007.
- [20] Lu H N, Wei D B, Jiang Z Y, et al. Modelling of size effects in microforming process with consideration of grained heterogeneity [J]. Computational Materials Science, 2013, 77: 44-52.
- [21] Jin C. Numerical simulation of welding process [M]. Beijing: Science Press, 2017.
- 金成. 焊接过程的数值模拟 [M]. 北京: 科学出版社, 2017.
- [22] Bonazzi E, Colombini E, Panari D, et al. Numerical simulation and experimental validation of MIG welding of T-joints of thin aluminum plates for top class vehicles [J]. Metallurgical and Materials Transactions A, 2017, 48(1): 379-388.
- [23] Farias R M, Teixeira P R F, Araújo D B, et al. Thermo-mechanical analysis of the MIG/MAG multi-pass welding process on AISI 304L stainless steel plates [J]. Journal of the Brazilian Society of Mechanical Sciences and Engineering, 2017, 39(4): 1245-1258.
- [24] Gazizulin D, Klein R, Bortman J, et al. Towards

- efficient spall generation simulation in rolling element bearing [J]. *Fatigue & Fracture of Engineering Materials & Structures*, 2017, 40(9): 1389-1405.
- [25] Jiang Z Y, Lu H N, Wei D B, et al. Finite element method analysis of micro cross wedge rolling of metals[J]. *Procedia Engineering*, 2014, 81: 2463-2468.
- [26] Chan W L, Fu M W, Lu J, et al. Modeling of grain size effect on micro deformation behavior in micro-forming of pure copper [J]. *Materials Science and Engineering: A*, 2010, 527(24/25): 6638-6648.
- [27] Wu G C, Li Y F, Pan X D, et al. Numerical simulation of fatigue damage and shape instability behavior of steel 40Cr by the damage-coupled crystal plastic model [J]. *Strength of Materials*, 2017, 49(1): 118-124.

Numerical Simulation on Laser Quenching of Stainless Steels with Grain Heterogeneity

Chen Zhengwei, Li Chang*, Gao Xing, Gao Hexin, Han Xing

School of Mechanical Engineering and Automation, University of Science and Technology Liaoning, Anshan, Liaoning 114051, China

Abstract

Objective Laser quenching has the advantages of small thermal deformation and thermal stress, short process cycle, stable and controllable quality, and high treatment efficiency. It can effectively improve the surface wear resistance, corrosion resistance, and fatigue resistance of mechanical parts. Recently, laser quenching has been widely used in many fields, such as automotive, aerospace, and mold. The macroscopic properties of a matrix material are the statistical results of all microscopic grains, and the mechanical properties are determined by the final state of all microscopic grains. The key to achieving precise control of the mechanical properties of the matrix is to optimize the microstructure during laser quenching. Therefore, to reveal the microevolution mechanism of the matrix in the laser quenching process is of great significance for optimizing the microstructural characteristics in the process. Laser quenching is a complex multi-field coupling process, and the microstructure changes instantaneously during the laser quenching process. It will consume a considerable amount of efforts to determine the laser quenching microevolution mechanism through repeatable experiments and traditional numerical simulation methods. In this study, a laser quenching model considering grain heterogeneity was developed on the ABAQUS platform with the Python script. This approach provided an effective method to reveal the laser quenching mechanism at the microcrystalline scale.

Methods First, a random microcrystalline structure model for the matrix was established by the Voronoi tessellation method. Then, the unquenched matrix nano-indentation test was conducted with a Keysight Nano Indenter G200 nano-indentation tester. The test results showed that the grains in the unquenched matrix were inhomogeneous (Fig. 3). The grain non-uniformity coefficient was calculated from the nano-indentation measurement results according to Eq. (8) and analyzed using statistical methods. The analysis results showed that the grain non-uniform coefficient obeys a normal distribution [Fig. 4(a)]. According to the grain non-uniformity coefficient, the grains in the unquenched matrix can be divided into seven types. After considering the sample points and the experimental errors, the grain non-uniformity coefficient distribution was standardized [Fig. 4(b)]. The mechanical properties of each type of grain were calculated according to the grain non-uniformity coefficient [Eq. (9)]. Finally, a Python script was used to randomly assign various material attributes to Voronoi cells in the unquenched matrix according to the grain non-uniformity coefficient after treatment (Fig. 5). A thermo-mechanical coupling model for the laser quenching process of SUS301L-HT stainless steels was established. The temperature field and thermal stress field were calculated.

Results and Discussions During the laser quenching process, the matrix rapidly produces temperatures and thermal stresses under the action of a high-energy laser. The temperature field of the matrix diffuses from the spot center to the surrounding. The matrix is simultaneously subjected to the combined effects of heat radiation, heat convection, and heat conduction during the transfer process. Thus, the matrix temperature decreases gradually from the heat source center to the outside. The temperature field distribution is approximately symmetrical, with the

scanning track as the axis. The back of the heat source continuously inputted quantities of heat by heat conduction. Thus, the temperature gradient in the front of the heat source is larger than that at the back. After natural cooling for 300 s, the temperature of the matrix is close to room temperature. The change in the temperature field of laser quenching showed that the characteristics of rapid cooling of laser quenching are prominent (Fig. 7). The characteristics of the temperature field distribution of laser quenching are consistent with the experimental results (Fig. 8). The distribution of the thermal stress field in the matrix is similar to that of the temperature field. Due to the high temperature in the heat source center, the metal mechanical properties in the region are reduced. Thus, the value of the thermal stresses in the center of the heat source is relatively small. The thermal stress of each crystal grain in the matrix is different, and the thermal stress of adjacent grains in the matrix occurs a sudden change at the grain boundary. Therefore, the thermal stress of the entire matrix presents a non-uniform distribution similar to the random geometric structure of the grain boundary. A few grains in the matrix have high mechanical properties. Under the laser irradiation, the thermal stress of these grains is higher than the average level, reaching 1429 MPa. However, the stress level of most grains in the matrix is about 600 MPa. Therefore, it can be found that the part of the grains with a higher thermal stress only represents the thermal stress state of the grains themselves, and it has a little contribution to the thermal stress state of the entire matrix (Figs. 9 and 11).

Conclusions Because of the inhomogeneity of the grain mechanical properties in the matrix, a sudden change in the grain stresses occurs at the grain boundaries. The larger the difference in the mechanical properties between adjacent grains is, the more obvious the stress mutation at the grain boundaries is. The thermal stress isolines show a similar irregular distribution with the grain boundary random geometry for the entire matrix. The laser quenching model considering the grain inhomogeneity can effectively capture the temperature and thermal stress changes of each grain in the matrix during the quenching process.

Key words laser technique; laser quenching; grain heterogeneity; stainless steel; Voronoi model

OCIS codes 140.6810; 160.3900